Physics – Uspekhi **53** (6) 000 – 000 (2010)

REVIEWS OF TOPICAL PROBLEMS

PACS numbers: 71.15.Mb, 77.55. D –, **85.30. – z**

Application and electronic structure of high-permittivity dielectrics

T V Perevalov, V A Gritsenko

DOI: 10.3367/UFNe.0180.201006b.0587

Contents

Abstract. Major applications of high-permittivity dielectric materials in silicon devices are reviewed. The basics and software implementations of the electron density functional method are considered. Results of first-principle calculations of the electronic structure are analyzed for the three most important and promising high-permittivity dielectrics, Al_2O_3, HfO_2, and TiO_2.

1. Introduction

One of the current priorities in science is the development of advanced materials for microelectronics. The basic dielectric material of modern microelectronics is silicon dioxide (SiO_2). However, the general fundamental trend in microelectronics toward increasing information capacity and speed of silicon devices requires that SiO_2 (with the dielectric constant $\varepsilon = 3.9$) be replaced by dielectrics with a higher dielectric constant (so-called alternative, or high-k, dielectrics). Candidates for alternative dielectrics are transition and rare-earth metal oxides, such as HfO_2, ZrO_2, Y_2O_3, La_2O_3, Er_2O_3, Gd_2O_3, and Sc_2O_3, as well as $SrTiO_3$, $HfSi_xO_y$, TiO_2, and Ta_2O_5.

Advances in the field of microelectronics heavily rely on understanding the electronic structure of solids, which makes this topic the subject of intense theoretical and experimental studies. A powerful, and sometimes the only means of obtaining detailed knowledge of processes at the atomic level is the use of quantum mechanical methods that model the electronic and atomic structure. However, because of the complex atomic structure of alternative dielectrics, the electronic structure of these multielectron systems is very difficult to study theoretically. Significant advances in this area were made due to the development of a self-consistent theory of the ground state of an inhomogeneous electron gas by Hohenberg–Kohn–Sham [1, 2], the so-called density functional theory (DFT). The basic ideas of this approach were described in Kohn's Nobel lecture [3]. This method allows using the first-principle approach to the quantitative analysis of the diverse properties of and phenomena in solids that are inaccessible to experimental investigation. We recall that first-principle calculations neither involve fitting parameters nor use phenomenological models, and their only input information is the number of an atom in the periodic table, i.e., the number of electrons in an atom and its atomic number. Currently, with the advent of powerful computers, virtually all ordered systems, as well as many disordered systems and interfaces, have become accessible to calculation. As a result, band calculations play an increasingly large role in understanding the physics of complex systems and phenomena and in elucidating the origine of quantitative differences between qualitatively similar systems. To date, the electrical properties of crystals have mostly been calculated using the DFT.

A major problem with practically all known alternative dielectrics is prohibitively high leakage currents through the film of a high-k dielectric. In the absence of defects, electron transport is limited by the tunneling injection of electrons and holes at junctions. The tunneling injection current flowing by the Fowler–Nordheim mechanism depends exponentially on the effective mass of carriers in the dielectric. Using theoretical values for the electron and hole masses in a high-permittivity dielectric, admissible parameters can be estimated for the corresponding structures. In addition, first-principle quantum mechanical simulations provide estimates for energy barriers, in particular, for the energy gap width. All this is the basis for the first-principle calculations of high-k dielectrics.

TV Perevalov, V A Gritsenko Rzhanov Institute of Semiconductor Physics, Siberian Branch of the Russian Academy of Sciences, prosp. Lavrent'eva 13, 630090 Novosibirsk, Russian Federation
Tel. (7-383) 333 38 64
E-mail: timson@isp.nsc.ru; grits@isp.nsc.ru

Received 20 April 2009, revised 26 August 2009
Uspekhi Fizicheskikh Nauk **180** (6) 587 – 603 (2010)
DOI: 10.3367/UFNr.0180.201006b.0587
Translated by E G Strel'chenko; edited by A M Semikhatov

Real high-k dielectrics usually contain defects that act as traps for charge-carrying electrons and holes. While information on the electronic structure of defects can be deduced from the experimental characteristics of high-k films, its correct interpretation is a nontrivial task. Volt–ampere characteristics are usually interpreted in terms of a particular phenomenological model (for example, the Pool–Frenkel model or multiphonon ionization) with a number of adjustable parameters, in particular, the tunneling effective mass. Hence, the electron and hole effective masses obtained from quantum mechanical simulation allow a more accurate interpretation of experimental results on charge transfer in high-k dielectrics.

The purpose of this paper is to introduce the reader to the basic applications of high-k dielectrics in silicon devices and to review the first-principle results on Al_2O_3, HfO_2, and TiO_2, three of the most important silicon device materials. Aluminum oxide (Al_2O_3) is a potential material for flash memory applications, HfO_2 is a candidate for a subgate dielectric in silicon devices with the designed standard thickness 45 nm, and TiO_2 is of great potential interest as a subgate dielectric for next-generation devices with a design standard of 32.20 nm.

The content of this review is briefly summarized as follows. Section 2 discusses the key applications of high-k dielectrics in silicon devices. In Section 3, the basic methodological DFT concepts are introduced, and two widely used program packages for the DFT calculation of the electronic properties of solids are briefly discussed. The subsequent sections present simulation results for the electronic structure of α- and γ-Al_2O_3 (Section 4); cubic, tetragonal, and monoclinic HfO_2 (Section 5); and rutile TiO_2 (Section 6). The calculated properties include band and phonon spectra, electron and hole effective mass tensors, total and partial densities of states, and charge density distributions. Special attention is given to comparing the calculated results with experimental data and previous calculations. An analysis of the electronic structure calculations and a discussion of further research on high-k dielectrics conclude the paper.

2. The use of high-permittivity dielectrics in silicon devices

The charge in a metal–insulator–semiconductor (MIS) inversion-channel transistor is proportional to the capacity of the condenser formed by the gate, the subgate dielectric, and the silicon substrate. The larger the capacity is, the larger (at a given gate potential) the charge in the inversion channel, the higher the channel conductivity, the steeper the I–V curve, and the higher the speed of the transistor. The capacity C of a plane condenser is given by

$$C = \frac{\varepsilon\varepsilon_0 S}{d}\,, \tag{1.1}$$

where ε_0 is the dielectric constant of the vacuum, S is the condenser area, and d is the thickness of the dielectric. The charge Q induced by a voltage V on the plates of a condenser of a capacity C is given by

$$Q = C\,V\,. \tag{1.2}$$

The information capacity of microcircuits increases in accordance with scaling rules, such that decreasing the length of the channel increases the capacity of the subgate dielectric. The first dielectric to be universally used in silicon microcircuits was silicon oxide (SiO_2, $\varepsilon = 3.9$). Thermal SiO_2 has been used for almost half a century as a subgate dielectric in MIS-field transistors. The thickness of SiO_2 in the first silicon MIS transistors was ≈ 100 nm. As the channel of the MIS transistor decreases in length, the capacity increases due to the decreasing thickness of the subgate dielectric. But there is a physical limitation on how thin the subgate dielectric can be. At present (2010), leading companies routinely use the design standard of 65 nm, for which the subgate SiO_2 has the thickness 1.0 – 1.2 nm. Changing to the design standard of 45 nm requires a further increase in the capacity of the subgate dielectric. However, further thinning the subgate oxide leads to unacceptably large tunneling leakage currents. The admissible leakage current is at a level of 1 A cm^{-2}. High leakage currents prohibitively add to the dissipation of power and decrease the slope of the transistor's I–V curve as a result of minority carriers being extracted from the inversion channel to the gate.

Since 2000, thermal SiO_2 has given way to silicon oxynitride SiO_xN_y ($\varepsilon \approx 5$) as a subgate dielectric. The prognosis is that low-power-consumption logic circuits (portable devices such as notebooks, digital photo cameras, and mobile phones) will be using SiO_xN_y until 2016 [4]. In such devices, the leakage current at the voltage of 1 V should not exceed 1.5×10^{-2} A cm^{-2}. In high-speed high-dissipation devices, in particular, microprocessors, using SiO_xN_y does not solve the scaling problem.

A radical way to suppress the tunneling leakage currents is to replace the oxide or oxynitride of silicon by a dielectric with a high dielectric constant (a high-k dielectric) [5]. In this terminology, the dielectric constant is denoted by the symbol k. This terminology was suggested by American engineers and is common in microelectronics. In physics, the dielectric constant is denoted by the symbol ε. Materials currently being considered for use as high-k subgate dielectrics in MIS devices include hafnium oxide HfO_2 ($\varepsilon \approx 25$), zirconium oxide ZrO_2 ($\varepsilon \approx 25$), hafnium silicate $HfSiO_4$ ($\varepsilon \approx 15$), zirconium silicate $ZrSiO_4$ ($\varepsilon \approx 15$), hafnium oxynitride HfO_xN_y ($\varepsilon \approx 15$), and aluminum oxide Al_2O_3 ($\varepsilon \approx 10$) [6].

Figure 1 schematically shows the structure of Si/SiO_2/polysilicon (poly-Si) with the oxide thickness 1.0 nm, Si/high-k dielectric/poly-Si with the high-k dielectric thickness 4.0 nm, and Si/SiO_2/high-k dielectric/poly-Si with the SiO_2 thickness 0.5 nm and the high-k dielectric thickness 3.0 nm. The capacity of the dielectric layer is the same for all three structures. The energy diagrams in the figure illustrate the passage of tunneling current in the corresponding structures. The large physical thickness of the high-k dielectric results in the suppression of the tunneling current.

We list the requirements for high-k dielectrics when used as subgate dielectrics [6]:

- a large value of the static dielectric constant ($\varepsilon \geqslant 10$);
- a wide band gap ($E_g > 3$ eV);
- high electron and hole barriers at the silicon–dielectric interface (to ensure low leakage currents);
- a low concentration of traps (to secure a stable threshold voltage and low leakage currents);
- chemical stability in terms of interaction with silicon, silicon oxide, and the gate material;
- compatibility with current technology.

The simultaneous requirements of a high dielectric constant and a wide band gap contradict each other. As seen

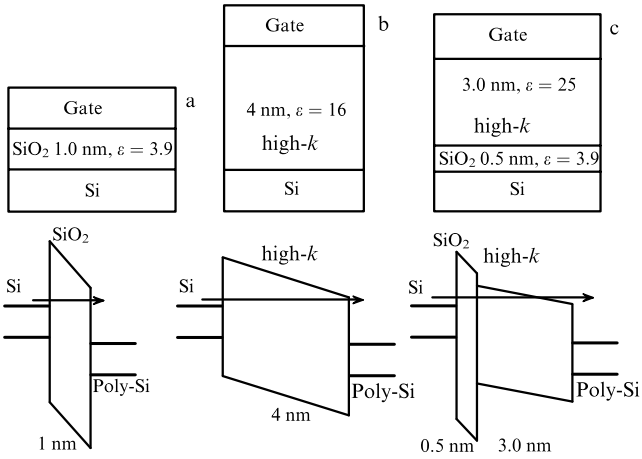

Figure 1. Structures with an equal capacitance of a dielectric layer: (a) Si/SiO_2/poly-Si, (b) Si/high-k dielectric/poly-Si, and (c) Si/SiO_2/high-k dielectric/poly-Si. An energy diagram under each structure illustrates tunnelling currents through the dielectric layer.

from Fig. 2, the higher the dielectric constant is, the narrower the band gap of a dielectric. With this condition, the spectrum of acceptable alternative dielectrics is limited to those with not too large dielectric constants. Materials with extremely high dielectric constants, for example, barium titanate ($BaTiO_3$, $\varepsilon \sim 1000$), have too small band gaps.

Potential energy barriers for electrons and holes at the dielectric–contact interface respectively determine the electron and hole injection currents. For a dielectric to be able to block these currents, the potential barriers should exceed 1 eV. Figure 3 presents a schematic for electron and hole potential barriers at the interface between silicon and known high-k dielectrics.

Thermal oxide SiO_2 is also used as an insulator in memory capacitors used in static and dynamic random-access memory (RAM) [6]. The capacity of RAM is increased by decreasing the area of storage condenser cells. For this, it is necessary to decrease the thickness of the dielectric layer in order that the electric capacity of the storage condensers not decrease. But a small oxide thickness increases the leakage current of the storage condenser, leading to the spread of the charge accumulated on the condenser plates. The leakage current of a RAM storage capacitor should not exceed 10^{-7} A cm^{-2}. An alternative solution to RAM scaling is to use a high-permittivity dielectric. Hence, increasing the information

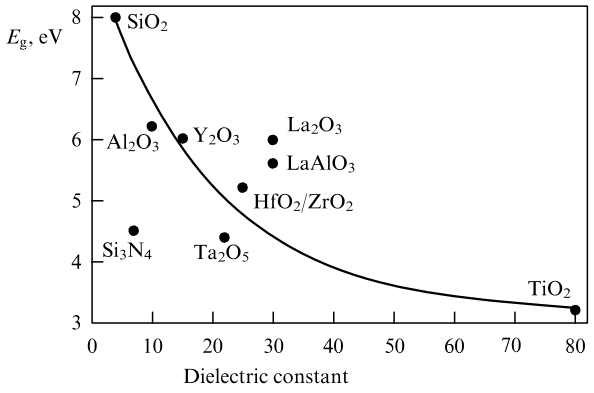

Figure 2. Band gap width vs. static dielectric constant for a dielectric.

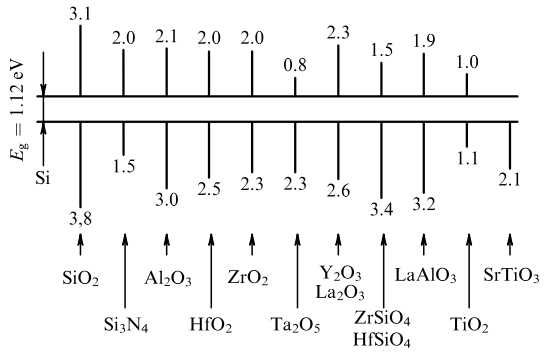

Figure 3. Energy diagram of the interface between silicon and dielectrics used in silicon devices, with the potential barriers for electrons and holes indicated (in electron volts).

capacity of RAM requires using high-k dielectrics. At present, RAM capacitors use silicon nitride Si_3N_4 ($\varepsilon = 7.0$) instead of SiO_2. The nitride and oxynitride of silicon are often called middle-k dielectrics. At present, Al_2O_3 ($\varepsilon = 10$), Ta_2O_5 ($\varepsilon = 22$), HfO_2 ($\varepsilon = 25$), and TiO_2 ($\varepsilon \approx 80$) are considered promising candidates for RAM isolators.

A third major application of high-permittivity dielectrics is as the upper blocking layer in silicon flash memory. Today, intense research is geared to achieving the industrial production of flash memory using polysilicon–oxide–nitride–oxide–semiconductor (PONOS) structures. Such a flash memory element is an MIS transistor with a multilayer dielectric and a variable threshold voltage (Fig. 4a). As a the storage medium, a flash memory element employs amorphous Si_3N_4 with a high (10^{19} cm^{-3}) density of deep (≈ 1.5 eV) electron and hole traps. The silicon nitride is separated from the silicon substrate by a tunneling oxide (SiO_2) with the thickness 1.8 – 5.0 nm. To block the parasite injection of electrons and holes from the gate into the silicon nitride, an oxide layer is placed between the two. Common PONOS structures use silicon oxide as the blocking layer.

Applying a negative potential (10^{-3} s voltage pulse) to the gate causes the injection of holes from the silicon substrate through the tunneling oxide to the silicon nitride, followed by their capture by deep hole traps (Fig. 4b). After turning off the gate voltage, the holes that have accumulated in the silicon nitride induce a conducting inversion channel in the transistor. The transistor makes the transition to the open state, which is considered to be the logical '0'. Owing to the extremely long lifetime of (localized) trapped holes, the logical '0' can be stored for 10 years at 85 °C without any energy consumption (unlike the usual trigger). This is how information is programmed in a flash memory cell. A flash matrix is made up of a large number of flash cells. The way to erase the information is by applying a positive pulse to the gate (Fig. 4a), which causes electrons in the silicon to be injected through the tunneling oxide and be caught by deep traps in the silicon nitride. Turning the voltage off leaves the nitride with a negative charge, which acts to induce an enrichment layer in the silicon (holes). The conducting channel disappears, meaning that the storage transistor is closed. The situation that emerges is that of the logical '1'. Such is the operation of a usual nitride-based PONOS flash-memory cell.

The authors of Refs [7, 8] proposed using high-k dielectrics, for example, Al_2O_3 or ZrO_2, instead of SiO_2 as

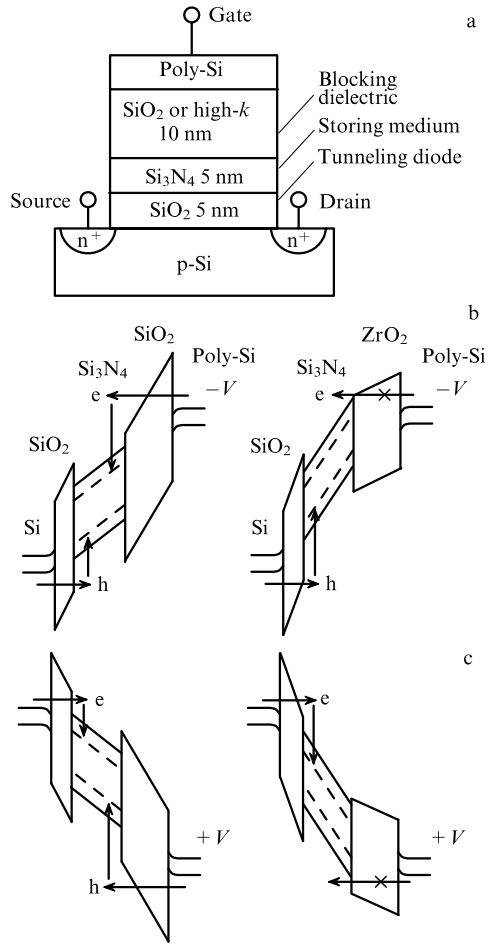

Figure 4. PONOS (flash) memory cell (a) and energy diagrams of a PONOS memory cell with a blocking layer of SiO_2 or ZrO_2 in the write (b) and erase (c) operation regimes.

blocking layers in PONOS structures. There is also a suggestion [9, 10] to use a blocking high-k dielectric in a flash memory cell with silicon nanoclusters as a storing medium. Figures 4b, c present energy diagrams for a PONOS memory element with a ZrO_2 layer as a blocking layer in the write–erase regime. Because the dielectric constant of ZrO_2 ($\varepsilon = 25$) is much larger than that of SiO_2 ($\varepsilon = 3.9$), the electric field in the blocking high-k dielectric is (for equal amplitudes of the program/erase pulse) smaller than in the blocking SiO_2. Hence, the voltage decrease across the blocking high-k dielectric is less than for the blocking SiO_2. The result of this decrease is a larger voltage drop across the tunneling oxide, and hence a larger field in the oxide. The increased field increases the electron and hole tunneling injection rate from the silicon substrate, thus increasing the operation speed in the program/erase mode at a fixed thickness of the tunneling oxide. PONOS structures with blocking SiO_2 use tunneling thermal SiO_2 with the thickness 1.8 nm [11]. Replacing the blocking SiO_2 by a high-k dielectric allows the tunneling SiO_2 layer to be increased in thickness from 1.8 to 5.0 nm, while leaving the operation speed unchanged [12 – 16]. Increasing the thickness of the tunneling oxide increases the flash memory reliability in the information storing regime. Yet another advantage of using a blocking high-k dielectric is suppressing the parasite injection of electrons and holes from the gate due to a decrease in the electric field in the blocking high-k dielectric. Thus, using high-k dielectrics increases the operation speed, reliability, and useful yield, and hence decreases the cost of flash memory. A promising candidate for the blocking dielectric in PONOS structures — and accordingly a subject of intense recent study — is aluminum oxide, Al_2O_3 [17 – 19].

3. Electronic structure calculation methods for solids

3.1 Density functional method

The technological incorporation of high-k dielectrics requires a knowledge of their electronic structure and physical properties. A powerful means of studying high-k dielectrics is by using *ab initio* quantum mechanical methods to investigate electronic and atomic structures. In principle, by applying these methods to a polyatomic system, it is possible to calculate all of its properties that can be determined experimentally, and in fact those that cannot. In real life, however, the power of the non-empirical method depends on the available computer resources.

At present, one promising direction in quantum mechanical research is to use methods based on the DFT. The advantage of DFT methods compared to other methods that also include the exchange-correlation interaction is that the DFT they requires relatively limited computer resources to achieve sufficient accuracy. What principally distinguishes the DFT method is that it does not work by approximately solving the stationary Schrödinger equation to obtain the multielectron wave function of a molecular system as a function of 3N spatial coordinates but uses the electron density of an electron system to calculate its properties.

The foundations of the method were laid by Hohenberg, Kohn, and Sham [1, 2], who proved two important theorems. The first theorem states that for a system of electrons in an external field with the potential of a general form $V(\mathbf{r})$, the knowledge of the ground state electron density $\rho(\mathbf{r})$ determines the potential $V(\mathbf{r})$ uniquely (up to a physically meaningless constant). This statement is true for both nondegenerate and degenerate ground states. In the latter case, the density of any degenerate state is determined by the external potential $V(\mathbf{r})$. Because $V(\mathbf{r})$, as well as the number of electrons, is determined by $\rho(\mathbf{r})$, all the properties that follow from the form of the Hamiltonian are determined by the density $\rho(\mathbf{r})$. Hence, $\rho(\mathbf{r})$ determines the energies of the ground and excited states, and so on. The total energy of the electron system can be expressed as a density functional,

$$E[\rho(\mathbf{r})] = \int V(\mathbf{r})\,\rho(\mathbf{r})\,\mathrm{d}\mathbf{r} + T[\rho(\mathbf{r})] + V_{\mathrm{ee}}[\rho(\mathbf{r})]\,, \qquad (3.1)$$

where the first, second, and third terms in the right-hand side represent the interaction energy with the external field, the kinetic energy functional, and the electron–electron interaction energy functional.

The second theorem asserts that for a given $V(\mathbf{r})$, the ground state density $\rho_0(\mathbf{r})$ minimizes the total energy functional. Hence, given a sufficiently accurate knowledge of the sum of the second and third terms in $E[\rho]$, the ground state energy and density of any electron system can be found by minimizing $E[\rho]$, regardless of the number of electrons.

Along with a real system of interacting electrons with a density $\rho(\mathbf{r})$, Kohn and Sham introduced the notion of a

hypothetical system of noninteracting electrons with the same number of particles and the same density $\rho(\mathbf{r})$. The Hamiltonian $\hat{H}_s$ and kinetic energy $T_s[\rho]$ of this hypothetical system are given by

$$\hat{H}_s = \sum_i^N \left(-\frac{\hbar^2}{2m} \Delta_i \right) + \sum_i^N V_s(\mathbf{r}_i) , \tag{3.2}$$

$$T_s[\rho] = \left\langle \Psi_s \middle| \sum_{i=1}^N \left(-\frac{\hbar^2}{2m} \Delta_i \right) \middle| \Psi_s \right\rangle . \tag{3.3}$$

The exact solution for this system is the single-determinant wave function

$$\Psi_s = \frac{1}{\sqrt{N!}} \det[\varphi_1 \varphi_2 \dots \varphi_3] , \tag{3.4}$$

where the φ_i are the N lower eigenstates of the one-electron Hamiltonian $\hat{h}_s$,

$$\hat{h}_s \varphi_i(\mathbf{r}, \sigma) = \left[-\frac{\hbar^2}{2m} \Delta + V_s(\mathbf{r}) \right] \varphi_i(\mathbf{r}, \sigma) = \varepsilon_i \varphi_i(\mathbf{r}, \sigma) . \tag{3.5}$$

The functionals $T_s[\rho]$ and $J[\rho]$ are calculated using the exact wave function $\varphi_i(\mathbf{r}, \sigma)$ of the noninteracting system. Kohn and Sham then make the substitution

$$T\left[\rho(\mathbf{r})\right] + V_{ee}\left[\rho(\mathbf{r})\right] \equiv T_s[\rho] + J[\rho] + E_{xc}[\rho] , \tag{3.6}$$

$$J[\rho] = \int \frac{\rho(\mathbf{r}_1)\, \rho(\mathbf{r}_2)}{|\mathbf{r}_1 - \mathbf{r}_2|} \, d\mathbf{r}_1 \, d\mathbf{r}_2 , \tag{3.7}$$

where the exchange-correlation functional $E_{xc}[\rho]$ contains the difference between the exact kinetic energy functional and the functional $T_s[\rho]$, as well as the nonclassical part of the electron–electron repulsion.

Thus, the total energy functional reduces to the form

$$E\left[\rho(\mathbf{r})\right] = \int V(\mathbf{r})\, \rho(\mathbf{r})\, d\mathbf{r} + \int \frac{\rho(\mathbf{r}_1)\, \rho(\mathbf{r}_2)}{|\mathbf{r}_1 - \mathbf{r}_2|} \, d\mathbf{r}_1 \, d\mathbf{r}_2 + T_s\left[\rho(\mathbf{r})\right] + E_{xc}\left[\rho(\mathbf{r})\right] . \tag{3.8}$$

The problem of finding the minimum of energy functional (3. 8) under the condition of a fixed number of particles is solved by the method of Lagrange multipliers. The matching condition between the Euler equations for a real interacting and a noninteracting electron system leads to the condition

$$V_s(\mathbf{r}) = V(\mathbf{r}) + \frac{\delta J[\rho]}{\delta \rho} + \frac{\delta E_{xc}[\rho]}{\delta \rho} . \tag{3.9}$$

Therefore, the one-electron wave functions are obtained from the solution of Kohn–Sham equation (3. 5) with the potential $V_s(\mathbf{r})$ given by Eqn (3.9). The energy of a real interacting electron system is then written as

$$E = 2 \sum_{i=1}^{N/2} \varepsilon_i - J\left[\rho(\mathbf{r})\right] - \int \frac{\delta E_{xc}[\rho]}{\delta \rho} \, \rho(\mathbf{r}) \, d\mathbf{r} + E_{xc}\left[\rho(\mathbf{r})\right] . \tag{3.10}$$

The exact form of the exchange-correlation functional $E_{xc}[\rho]$, a necessary requirement for specific calculations, is never known, but there is a number of approximate expressions, using which in calculations yields results in excellent agreement with experimental data. One of the most widely used approaches for describing $E_{xc}[\rho]$ in the case of slowly varying density is the local density approximation (LDA) developed by Kohn and Sham in 1965. An improved and more accurate level of approximation for the exchange-correlation energy is provided by the generalized gradient approximation (GGA). To date, various researchers have developed a large number of exchange correlation functionals for the LDA and GGA methods. The reader is referred to Ref. [20] for more details.

3.2 Pseudopotential approximation

Inner atomic-shell electrons are not active in the formation of chemical bonding in solids because their binding energy with nuclei, of the order of tens or even hundreds of electron-volts per electron, is much larger than the average interatomic interaction energy. The wave functions of these electrons contribute little to the crystal potential and to the final wave function, and at the same time strongly oscillate in the strong potentials near the atomic cores. Therefore although electron wave functions can be expanded in terms of a plane-wave basis in accordance with the Bloch theorem, it takes a very larger number of plane waves to expand strongly bound inner orbitals and valence electron wave functions rapidly oscillating near the nuclei. A calculation including all electrons would require a tremendously large plane-wave basis, imposing heavy requirement on computer resources and time. Using the pseudopotential approximation greatly reduces the size of the plane-wave expansion basis for electron wave functions. In this approximation, the electrons in inner atomic shells and the strong ionic potential are replaced with a weaker 'pseudopotential,' and real wave functions, with 'pseudowave functions.' The pseudopotential is constructed such that its scattering properties and changes in the phase of the pseudowave function are identical to those of the valence wave function, whereas the radial component of the pseudowave function has no nodes in the near-nucleus region. Outside the nucleus region, the potential and pseudopotential are identical and their scattering effects are indistinguishable [21].

3.3 Density functional theory in electronic structure calculation methods

Presently, a variety of special-purpose software packages using the DFT can be used to calculate the electronic structure of molecules and periodic systems (crystals). One example is QUANTUM ESPRESSO [22, 23], where the Bloch functions of electrons in a crystal are sought by expanding in plane waves as basis functions. The crystal structure is specified by specifying the unit cell, and the translation symmetry is included through boundary conditions. For each type of calculation, the coordinates of atoms in and the parameters of the unit cell are specified, as are the pseudopotentials for each atomic species.

Another powerful quantum mechanical simulation package is ADF BAND (ADF for Amsterdam density functional). The ADF program is intended for calculating the electronic structure of atoms and molecules. BAND, a separate part of the ADF package, calculates periodic systems such as atomic chains, atomic layers, and bulk crystals [24]. The basis functions used are numerical orbits (NOs) and Slater-type orbitals (STOs). NOs are free atom wave functions calculated

with the Hermann–Skillman program. STOs have the form

$$X_{n,l,m} = A\, r^{n-1} \exp(-\xi r)\, Y_{lm}\,, \qquad (3.11)$$

where n is the effective principal quantum number. The simultaneous presence of NOs and STOs makes the basis set variationally flexible, enabling highly accurate calculations even with a small number of basis functions. The calculation of molecular orbits involves only the atomic orbitals of valence electrons, and inner atomic shells are frozen. However, their contribution to the crystal potential is included explicitly rather than through the pseudopotential.

4. Electronic structure of α- and γ-Al_2O_3

Corundum (α-Al_2O_3) is the most widely used and the most practically important crystalline modification of aluminum oxide. Among the many metastable crystalline modifications (the so-called transition aluminum oxides) [25], γ-Al_2O_3 is especially interesting as one of the most important and widely used catalytic materials. For use in silicon devices, amorphous Al_2O_3 is synthesized by atomic layer deposition (ALD) [26]. Densification of Al_2O_3 films is achieved by annealing. It was reported in [8] that amorphous Al_2O_3, when annealed, undergoes a transition to a crystalline γ phase. Thus, the electronic structure of γ-Al_2O_3 and, in particular, its electron and hole effective masses are currently a topical subject of study for applications in silicon devices.

The technological importance of aluminum oxide has stimulated numerous attempts toward understanding its electronic properties. The experimental methods that were used to study the electronic structure of α-Al_2O_3 are described in Refs [27 – 33]; there is also a large amount of literature on the use of various computational methods [33 – 45] for this purpose. Admittedly, however, contradictory results, both experimental and theoretical, are found among different studies. γ-Al_2O_3 has received much less attention [44 – 50], partly due to its more complex crystal structure and partly because of its narrower application range. In this review, we present simulation data on the electronic structure of α-Al_2O_3 and γ-Al_2O_3 and compare calculated and experimental results.

The unit cell of α-Al_2O_3 is rhombohedral ($R3cR$), contains 10 basis atoms, and has the lattice constants $a_i = 5.160$ Å and $\theta_i = 55.286°$ (Fig. 5a). The oxygen atoms are four-fold coordinated by aluminum ones. The aluminum atoms are coordinated by six oxygen atoms, with their three first- and three next-nearest at the respective distances 1.866 Å and 1.983 Å.

For γ-Al_2O_3, it is known that it has a defect spinel structure with vacancies at cation sites. Because of a large number of disagreements in both experimental and theoretical results (see Refs [49 – 52] for brief reviews), it has long been a subject of debate whether Al vacancies are located in octahedral or tetrahedral positions. A comprehensive experimental and theoretical study of the γ-Al_2O_3 crystal structure in [51] has recently showed the nonspinel sites to be populated in this material. However, the structure proposed by the authors of Ref. [51] has a very large atomic basis and hence requires considerable computer resources. In this work, we therefore follow the suggestion in Ref. [53] and assume that γ-Al_2O_3 has a 40-atom unit cell obtained from a spinel structure with two cation vacancies occupying octahedral sites and spaced maximally apart (Fig. 5c). A similar γ-Al_2O_3 model was used

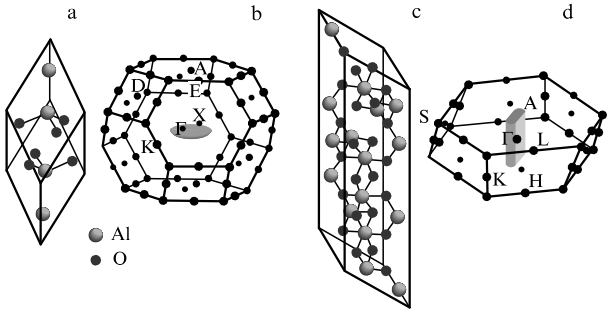

Figure 5. Trigonal 10-atom unit cell of α-Al_2O_3 (a) and 40-atom unit cell of γ-Al_2O_3 (b), with their respective Brillouin zones (c, d). Symmetry points and constant energy surfaces near the top of the valence band are marked.

in Refs [43, 48]. The equilibrium lattice constants were calculated as $a_1 = 5.647$ Å, $a_2 = 5.612$ Å, $a_3 = 16.778$ Å and $\theta_1 = 59.79°$, $\theta_2 = 55.24°$, $\theta_3 = 59.67°$. The Al atoms are six- and fourfold coordinated by O atoms. Because of the presence of cation vacancies in the γ-Al_2O_3 structure, its O atoms are coordinated by three or four Al atoms.

Electronic structure calculations for α-Al_2O_3 and γ-Al_2O_3 are performed with the software package ESPRESSO using the electronic configurations [Ne] $3s^2 3p^1$ for Al and [He] $2s^2 2p^4$ for O, where [Ne] and [He] are core states. The core electrons are included by using ultrasoft pseudopotentials borrowed from Ref. [23]. The criterion for selecting a pseudopotential is appropriate values of the structural parameters of the α-Al_2O_3 unit cell, which means agreement with the known experimental data. The selection procedure consists of a series of calculations on the structural relaxation of the α-Al_2O_3 unit cell for various pseudopotentials. It is found, in agreement with Ref. [39], that pseudopotentials with a GGA exchange-correlation functional overestimate lattice constants by $\leqslant 1\%$, whereas their LDA counterparts underestimate them by $\approx 2\%$. The way to parameterize the pseudopotential is chosen based on the idea that the calculated total energy of a relaxed unit cell should be a minimum. The electronic structures of α-Al_2O_3 and γ-Al_2O_3 are calculated using a pseudopotential with the GGA exchange-correlation functional in the parametrization of Perdew and Burke (PB).

Figure 6 presents band structure results for α- and γ-Al_2O_3 along the high-symmetry directions of their respective Brillouin zones (see Figs 5b, d). The zero energy level is taken at the top of the valence band. Both crystals are direct band gap insulators with the valence band top (and conduction band bottom) at the Brillouin zone point Γ. The result in Refs [38, 39] that α-Al_2O_3 is indirect is most likely due to the use of a nonrelaxed structure. Calculations for α-Al_2O_3 predict the existence of two bands close in energy ($\Delta E \approx 0.03$ eV), but very different in dispersion, at the top of the valence band, the upper and lower parts of which respectively correspond to light and heavy holes. The top of the valence band is calculated to be virtually flat.

The calculated band gaps E_g between the valence band top and the conduction band bottom are respectively given by 6.0 eV and 4.0 eV for α-Al_2O_3 and γ-Al_2O_3. These values disagree somewhat with other DFT calculations because of differences in computational methods and due to the sensitivity of E_g to the structural parameters. The experimental ranges of E_g are 7.5 – 9.5 eV for α-Al_2O_3 [31 – 33] and

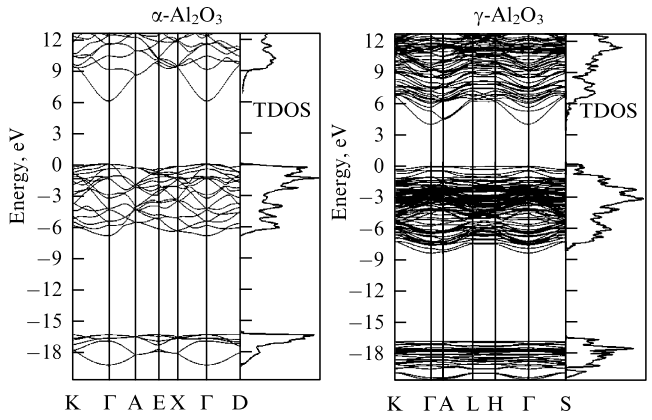

Figure 6. Band structures and total densities of states (TDOS) calculated for α-Al_2O_3 and γ-Al_2O_3.

7.2 – 8.7 eV for γ-Al_2O_3 [33, 51]. The discrepancy between the caclulation and the experiment is caused by a systematic underestimation of E_g in DFT calculations. Band gap estimates from the relation

$$E_g = (E_{tot}^{q=0} - E_{tot}^{q=+1}) - (E_{tot}^{q=-1} - E_{tot}^{q=0}) \qquad (4.1)$$

(where $E_{tot}^{q=0}$, $E_{tot}^{q=-1}$, and $E_{tot}^{q=+1}$ denote the total energies of the neutral, negatively charged, and positively charged structures) are respectively equal to $E_g = 8.2$ eV and $E_g = 6.0$ eV for α-Al_2O_3 and γ-Al_2O_3.

The valence bands of both crystals consist of two subbands separated by a wide ion gap (similar to SiO_2). Calculations of the partial density of states (PDOS) for α- and γ-Al_2O_3 show that the upper subband is formed by 2p electron states of oxygen, whereas the lower subbband is primarily formed (at the energy ≈ 20 eV) by oxygen 2s states with a small admixture of Al states. The conduction band is mainly formed by Al states (Fig. 7). The electron density of states near the bottom of the conduction band is very low. The band diagrams and PDOS spectra presented are in good agreement with previous DFT calculations [40 – 43, 47].

Figure 8 shows the calculated spatial distribution of the charge density $|\Psi(r,p)|^2$ for various energies in the valence band of α-Al_2O_3 in the plane of the O – Al – O bond. It is seen that the charge is distributed between two orbitals, O 2s, which is localized and binds O – Al, and O 2p, which is nonbinding. It follows from Fig. 8a that the lower valence subband is formed from oxygen 2s orbitals. In Fig. 8b, the shape of the charge density distribution and the fact that its orientation is along the Al – O bond are evidence for a binding oxygen σ orbital. This result is confirmed by PDOS calculations for α-Al_2O_3, which show a marked overlap of oxygen 2p orbitals with aluminum 3s and 3p states in the middle and near the bottom of the upper valence subband. Figure 8c shows the charge density distribution for energies near the top of the valence band in the direction perpendicular to the Al – O bond, presenting evidence for a nonbinding oxygen π orbital. The PDOS spetrum also shows that the top of the valence band is mostly formed by 2p electronic states. Similar charge density distribution patterns were observed in the valence band of SiO_2 [53, 54]. The nonbinding nature of the oxygen π oribital is also seen from the electron density distribution calculated for the upper valence band states of γ-Al_2O_3 [48]. Also according to Ref. [48], the charge concentration in γ-Al_2O_3 has a maximum at oxygen atoms near cation vacancies.

Table 1 presents the maximum and minimum values of the electron (m_e^*) and hole (m_h^*) effective masses in α-Al_2O_3 and γ-Al_2O_3 crystals. The effective masses were obtained by a quadratic approximation of the calculated dispersion $E(\mathbf{k})$ near the top of the valence band using the relation

$$m_{\alpha\beta}^{-1} = \frac{1}{\hbar^2}\frac{\partial^2 E(\mathbf{k})}{\partial k_\alpha \partial k_\beta} \qquad (4.2)$$

for the effective mass tensor.

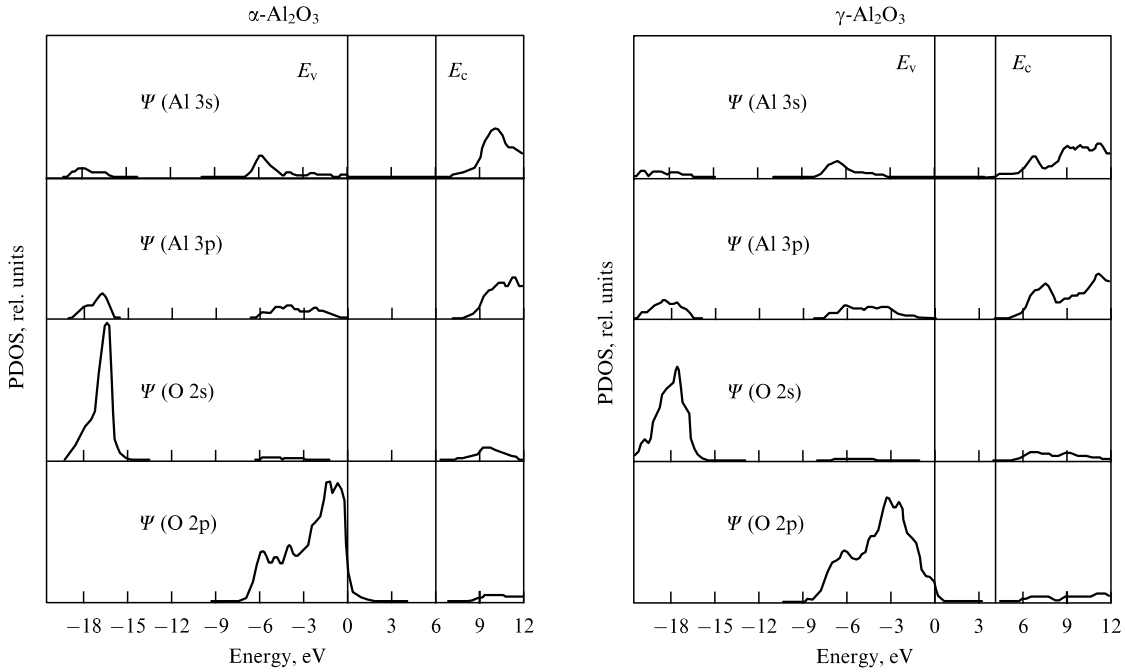

Figure 7. Calculated partial densities of states for α- and γ-Al_2O_3. The spectrum broadening is Lorentzian with the half-width $\sigma = 0.2$ eV.

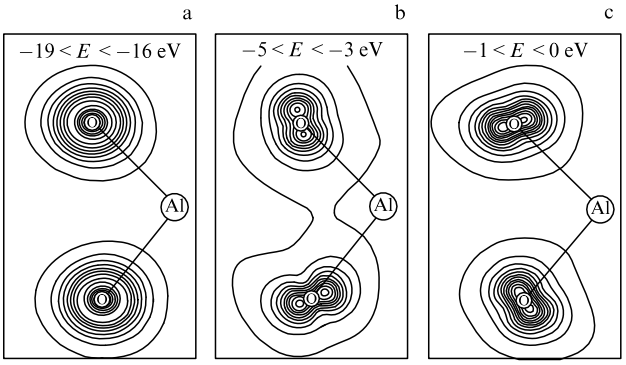

Figure 8. The calculated spatial charge density distribution in the valence band of α-Al_2O_3 in the plane of the O – Al – O bond.

Table 1. Maximum and minimum values of the electron (m_e^*) and hole (m_h^*) effective masses in crystals of α-Al_2O_3 and γ-Al_2O_3.

	α-Al_2O_3	γ-Al_2O_3
m_e^*/m_0	0.40 ($\Gamma \rightarrow$ A) 0.38 ($\perp \Gamma \rightarrow$ A)	0.40
m_h^*/m_0	7.5 ($\perp \Gamma \rightarrow$ A) 0.35 ($\Gamma \rightarrow$ A)	1.3 ($\Gamma \rightarrow$ K) $\gg 1$ ($\perp \Gamma \rightarrow$ K)

The electron effective masses in α-Al_2O_3 and γ-Al_2O_3 are virtually isotropic and equal, $m_e^* \approx 0.4m_0$. This value agrees with the experimental values of the tunneling electron effective mass in amorphous Al_2O_3: $m_e^* = 0.35m_0$, $m_e^* = (0.22-0.42)\,m_0$ [55], $m_e^* = 0.5m_0$ [56], and $m_e^* = 0.2m_0$ [57]. The hole effective mass exhibits strong anisotropy in both α-Al_2O_3 and γ-Al_2O_3. The experimental values of hole effective masses in α- and γ-Al_2O_3 are not available in the literature.

To describe the directional distribution of hole effective masses in α- and γ-Al_2O_3, constant-energy surfaces are constructed in k space near the top of the valence band and the bottom of the conduction band. In α-Al_2O_3, it is seen from the curvature of this surface near the valence band top that the hole masses have minimum values along the direction $\Gamma \rightarrow$ A and have maximum values (and are isotropic) in the plane perpendicular to this direction (Fig. 5b). For γ-Al_2O_3, it is only in the direction $\Gamma \rightarrow$ S that the isoenergetic surface has a noticeable curvature, and hence the material has a minimum effective mass (Fig. 5d). Perpendicular to $\Gamma \rightarrow$ S, the energy surface is virtually flat, which implies huge effective masses for the holes. Both in α-Al_2O_3 and γ-Al_2O_3, energy surfaces near the conduction band bottom have a spherical shape (not shown in Fig. 5), implying that the electron effective mass is isotropic.

An informative experimental tool for studying the electronic structure of solids is X-ray emission spectroscopy. Essentially, the method is to irradiate a solid (for example, Al_2O_3) to create vacancies at atomic levels such as Al 1s, Al 2p, and O 1s. A transition of valence band electrons to these states produces X-ray radiation, whose intensity is proportional to the transition probability and to the electron density of states in the valence band. It is generally assumed that the transition matrix element depends weakly on energy, and hence X-ray emission spectra reflect the distribution of the partial density of states in the valence band. The dipole approximation allows X-ray transitions under which the total orbital moment changes by unity, $\Delta l = \pm 1$. Transitions from 3s, 4s, and 3d states of Al in the valence band to aluminum $2p_{1/2,\,3/2}$ levels have the spectroscopic notation Al $L_{\mathrm{II,III}}$. Thus, the X-ray emission spectra of Al $L_{\mathrm{II,III}}$ reflect the distribution of the 3s, 4s, and 3d states of Al. The K spectra of Al reveal transitions from Al 3p states to the Al 2s level, meaning that the X-ray K emission spectra of Al reflect the distribution of Al 3p states. In oxygen, K emission spectra are observed for electron transitions from 2p to 1s levels and give information on the distribution of the partial density of states of oxygen 2p levels in the valence band [58].

Experiments studying the density of states in the conduction band rely on X-ray absorption spectra or the spectral dependence of quantum yield. The absorption spectra reflect transitions from deep atomic levels to unoccupied states of the valence band. These transitions also obey the dipole selection rules. The spectral dependences of quantum yield reflect the partial density of states in the conduction band to within the dependence of the transition matrix element on energy [58].

Figure 9 uses a common energy scale (setting the energy origin at the top of the valence band) to present measurement results in Ref. [27] for X-ray emission spectra and quantum yield in α-Al_2O_3 and γ-Al_2O_3. A good agreement between the calculated partial density of states and the X-ray emission and absorption spectra is observed for the oxygen 2p orbitals and the oxygen K spectra. The mismatch in position between the calculated main peaks of the valence band and the corresponding experimental peaks is most likely due to the underestimated widths for all the subbbands of the valence band, a notorious weak point of DFT calculations. A good agreement between calculations and the X-ray K emission spectra of Al is observed only for the upper valence subbband. For α- and γ-Al_2O_3, the calculated PDOS peaks of Al 3p in the lower valence subband are more intensive than those in the upper, and much more intensive than those of their experimental counterparts. Interestingly, a similar disagreement with experiments was found for SiO_2 and Si_3N_4 in [59, 60]. The calculated partial density of states for Al 3s does not provide an adequate description of all the structural details of the experimental $L_{\mathrm{II,III}}$ spectrum of Al. In particular, the calculated spectrum of Al 3s lacks an upper peak at ≈ 3 eV. In SiO_2 and Si_3N_4, which show a similar disagreement, the upper peak in the valence band is thought to be associated with the 3d orbitals of Si and with nonlocal (bicentral) transitions [59]. It is beyond the scope of this paper to calculate the electronic structure of Al_2O_3 with the correct account of the contribution of Al 3d orbitals in order to describe X-ray emission spectra. It is noteworthy that according to the calculations in Ref. [59], the inclusion of 3d orbitals for Si has little effect on the electron and hole effective masses in SiO_2 and Si_3N_4.

In Fig. 10, the measured ultraviolet photoelectron spectra (UPSs) and X-ray photoelectron spectra (XPSs) of amorphous aluminum oxide (a-Al_2O_3) are compared with the calculations for α- and γ-Al_2O_3. The excitation of XPSs was performed by monochromatic Al K_α radiation with energy $\hbar\omega = 1486.6$ eV, whereas UPSs were excited by the HeII line with $\hbar\omega = 40.8$ eV from helium plasma. The calculated spectra are obtained by summing the partial densities of states of valence orbitals with weights equal to the corresponding photoionization cross sections taken from Ref. [61]. It follows from Fig. 10 that the calculated UPSs of α- and γ-Al_2O_3 and the experimental UPSs of α-Al_2O_3 agree well in

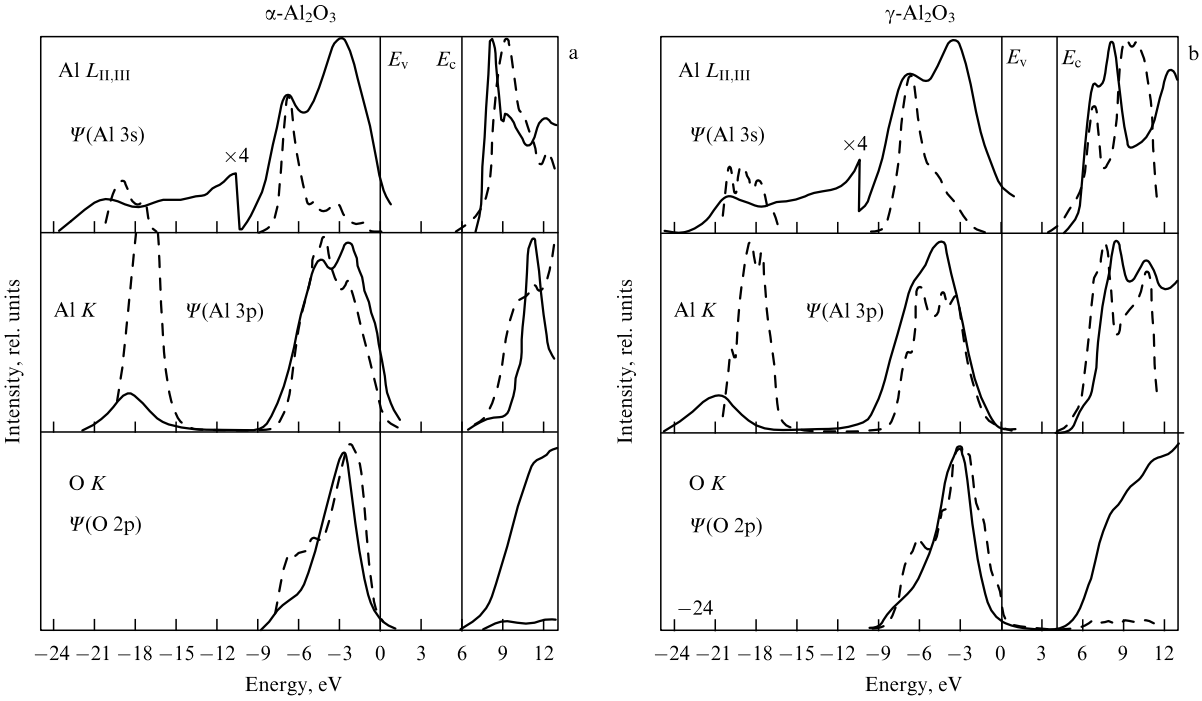

Figure 9. Experimental X-ray emission and absorption spectra of α-Al_2O_3 and γ-Al_2O_3 (solid lines) and the corresponding calculated densities of states (dashed lines) broadened in accordance with the Lotentzian with a halfwidth $\sigma = 0.4$ eV.

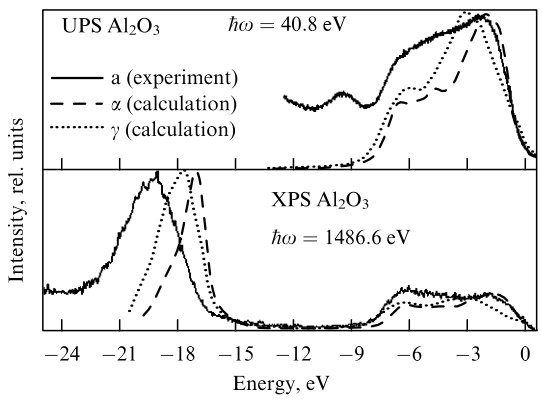

Figure 10. Experimental UPSs and XPSs of amorphous a-Al_2O_3 (solid lines). Dashed and dash-dotted lines are the corresponding calculated UPSs and XPSs for α-Al_2O_3 and γ-Al_2O_3 broadened in accordance with a Lorentzian with the halfwidth $\sigma = 0.4$ eV.

terms of the relative peak intensity. A similar agreement is observed for the measured and predicted X-ray spectra. The position mismatch between the main peaks is obviously due to the overestimated widths of both valence band subbands. The width difference between the experimental and predicted peaks may be due to the finite lifetime of a hole at core levels, a factor that leads to the broadening of experimental peaks. The inclusion of peak broadening processes (for example, the Auger process) requires a much more involved theoretical model.

To summarize, satisfactory qualitative agreement is observed between the calculated and measured results for the X-ray and ultraviolet spectra of Al_2O_3, allowing the conclusion that DFT band calculations are qualitatively correct in predicting the electronic structure of α-Al_2O_3 and γ-Al_2O_3. Also, α-Al_2O_3 and γ-Al_2O_3 have qualitatively similar electronic structures. Hence, the key aspects of the electronic structure of Al_2O_3 are determined by the short-range order in atomic arrangement (similarly to situations in SiO_2 and Si_3N_4).

The calculated high-frequency dielectric constant tensors ε^{e}_{ij} of α- and γ-Al_2O_3 can be written in Cartesian coordinates as

$$\varepsilon^{\infty}_{ij}(\alpha\text{-}Al_2O_3) = \begin{pmatrix} 3.22 & 0.0 & 0.0 \\ 0.0 & 3.22 & 0.0 \\ 0.0 & 0.0 & 3.19 \end{pmatrix};$$

$$\varepsilon^{\infty}_{ij}(\gamma\text{-}Al_2O_3) = \begin{pmatrix} 3.14 & -0.02 & 0.0 \\ -0.02 & 3.14 & 0.0 \\ 0.0 & 0.0 & 3.14 \end{pmatrix}.$$

We see that both crystals are slightly anisotropic in their optical properties. Slightly smaller values are given in [43]: $\varepsilon^{\infty} = 3.17$ for α-Al_2O_3 and $\varepsilon^{\infty} = 3.13$ for γ-Al_2O_3, although the value in Ref. [41] is $\varepsilon^{e}_{ij} = 3.86$ for α-Al_2O_3. The value $\varepsilon^{\infty}_{ii} = 3.2$ agrees with the measured refractive index $n = 1.8$ for α-Al_2O_3: $\varepsilon^{\infty} = n^2 = (1.8)^2 = 3.24$.

In Fig. 11, the spectra of the total phonon density of states calculated for α-Al_2O_3 and γ-Al_2O_3 are imposed on the experimental phonon spectrum of α-Al_2O_3 taken from Ref. [62]. The phonon spectrum of α-Al_2O_3 is calculated for a 30-atom hexagonal unit cell. The predicted and measured data for α-Al_2O_3 are in good qualitative agreement in terms of the number of peaks. The satisfactory agreement between the theoretical and experimental curves for the total phonon density of states allows concluding that the calculation model used describes interatomic interactions correctly. For the phonon density of states in γ-Al_2O_3, a marked broadening of the entire spectrum and a small shift to lower frequencies are observed.

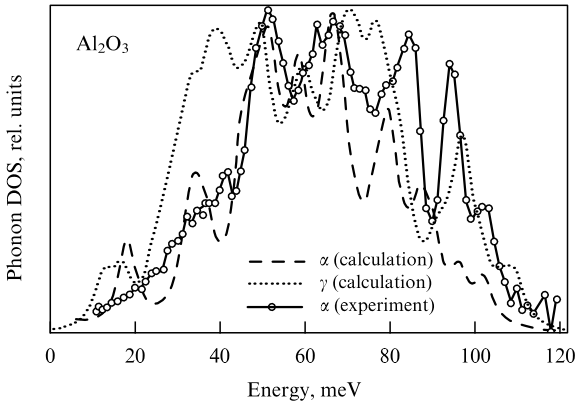

Figure 11. Experimental (solid line) and calculated (dashed line) phonon densities of states for α-Al_2O_3. Dash-dotted line shows the calculated phonon density of states for γ-Al_2O_3.

It is known that the large dielectric constant of high-k dielectrics is mainly determined by the lattice type. Low-stiffness bonds present in these crystals make the crystals susceptible to an electric field, whence a high polarizability and, accordingly, a higher dielectric constant. In other words, the high value of the static dielectric constant of high-k dielectrics is due to the presence of low-frequency natural vibrations, so-called soft modes, in the lattice. The expression for the low-frequency dielectric constant ε is

$$\varepsilon = n^2 + \frac{Ne^2 Z_T^2}{m\omega_{TO}^2}\,, \tag{4.3}$$

where n is the refractive index, N is the ion concentration, Z_T is the 'transverse' effective charge, and ω_{TO} is the frequency of transverse optical phonons. It follows from Fig. 11 that the Al_2O_3 lattice exhibits low-frequency natural vibrations (soft modes) in the frequency range below 50 MeV (400 cm^{-1}), which are absent from the natural spectrum of SiO_2 [62]. Clearly, just the presence of these modes results in the static dielectric constant of Al_2O_3 ($\varepsilon \approx 10$) being higher than that of SiO_2.

Figure 12 is an energy diagram for electron transitions in α-Al_2O_3, obtained with the approach developed for SiO_2 [63]. All energies are measured from the energy of an electron in a vacuum, which is above the bottom of the conduction band by $\phi^e = 2.0$ eV [56, 64]. The energies of the inner Al 1s and Al 2p levels were determined in Ref. [27] using X-ray photoelectron spectroscopy. The energies of the oxygen 2s and 2p levels are taken from Ref. [65]. The horizontal lines in the valence and conduction bands indicate the positions of the peaks in the density of states observed in X-ray transitions [27].

5. Electronic structure of HfO_2

At normal pressure, HfO_2 crystallizes in three structures: a low-temperature monoclinic phase (m-HfO_2), a tetragonal phase (t-HfO_2) at temperatures above 2000 K, and a cubic phase (c-HfO_2) above 2870 K [66]. Under normal conditions, crystalline HfO_2 exists in a monoclinic structure, which is why this phase has been most intensively studied [67, 68]. Some studies [69 – 72] report the formation of the cubic phase in thin films (10 – 50 nm) of HfO_2 (and ZrO_2) at temperatures around 200 °C. At temperatures from 300 to 600 °C, films in the

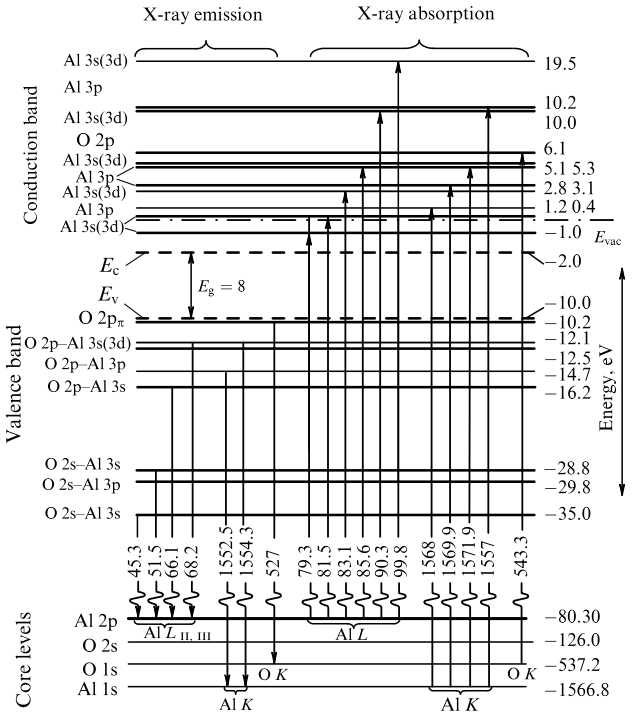

Figure 12. Empirical energy diagram of electron transitions in α-Al_2O_3.

thickness range 10 – 50 nm exhibit a tetragonal phase with markedly different parameters from those in the high-temperature bulk structure. A stable monoclinic phase is observed forming at film thicknesses > 500 nm.

In Fig. 13, the cubic, tetragonal, and monoclinic crystal structures of HfO_2 are shown together with their corresponding Brillouin zones (with symmetry points marked). The Bravais lattice of HfO_2 for the cubic system is a face-centered cubic cell (space group $Fm3m$). The atomic basis consists of one Hf and two O atoms, and the lattice constant is $a_i = 5.08$ Å [73]. For the tetragonal HfO_2, the unit cell is a regular square-based prism (space group $P4_2/nmc$). The atomic basis consists of two Hf and four O atoms, and the lattice constants are $a = 3.56$ Å and $c = 5.11$ Å [73]. In the cubic and tetragonal phases of HfO_2, O atoms are four-fold coordinated by Hf atoms, and Hf atoms are eight-fold coordinated by O atoms. For the monoclinic phase, the

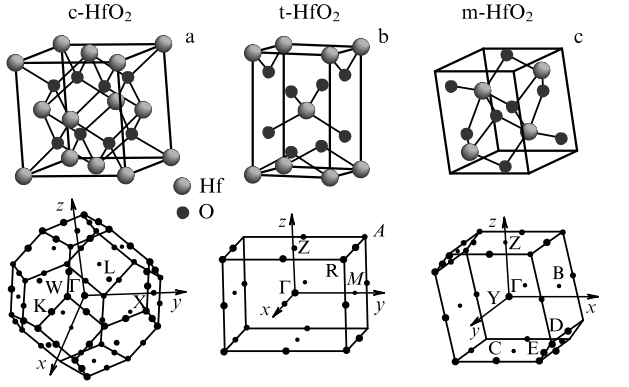

Figure 13. Crystal structure of cubic (a), tetragonal (b), and monoclinic (c) phases of HfO_2 and their respective Brillouin zones indicating a symmetry point.

atomic basis of the unit cell consists of three Hf and six O atoms (space group $P2_1/c$). The lattice constants are $a = 5.08$ Å, $b = 5.19$ Å, $c = 5.22$ Å, and $\theta = 99.77°$. The monoclinic phase involves two types of O atoms in terms of coordination, with the respective coordinate numbers 7 and 8.

The electronic structure of HfO_2 is calculated using the ADF BAND program. The respective number of basis functions per unit cell of the cubic, tetragonal, and monoclinic phases of Hf was 70, 150, and 300. Similar DFT calculations for the cubic, tetragonal, and monoclinic phases of HfO_2 were performed in [74] using a plane-wave basis set.

Figure 14 presents calculated band diagrams for the cubic, tetragonal, and monoclinic crystalline phases of HfO_2 for special points of its Brillouin zone. The zero energy is chosen to be at the top of the valence band. As the size of the atomic basis is increased, the band structure becomes noticeably more complicated, while remaining qualitatively the same for all three phases. The valence bands calculated for HfO_2 phases consist of three subbands separated by wide ionic gaps. For cubic HfO_2, the top of the valence band E_v and the bottom of the conduction band E_c are respectively at the X and Γ points of the Brillouin zone. For the tetragonal phase, E_v (E_c) is at the Γ (M) point, and for the monoclinic phase, E_v (E_c) is at the Γ (B) point. Therefore, all the three phases of HfO_2 are indirect dielectrics. The band gaps of the cubic, tetragonal, and monoclinic HfO_2 estimated from the difference between E_c and E_v, are respectively given by 3.2, 3.8, and 3.5 eV. Experimental values of E_g for amorphous HfO_2 are much higher and range from 5.3 to 5.9 eV depending on the source [75–78].

At the bottom of the conduction band of cubic HfO_2 at the Γ point, a doubly degenerate state is split along the direction $\Gamma \to X$ and not along $\Gamma \to L$. For tetragonal HfO_2, the top of the valence band is degenerate in the directions $A \to M$ and $Z \to A$. For monoclinic HfO_2, the electron states both at the top of the valence band and at the bottom of the conduction band are nondegenerate.

The electron and hole effective masses for the three crystalline phases of HfO_2 are listed in Table 2. It is seen that HfO_2 contains both heavy and light holes and that the hole effective masses have a wide spread in values ranging from $0.3m_0$ for cubic HfO_2 to $8.3m_0$ for tetragonal HfO_2. The conduction electron in all phases has close values, with both

Table 2. Electron (m_e^*) and hole (m_h^*) effective masses for cubic, tetragonal, and monoclinic HfO_2.

	Cubic phase HfO_2	Tatragonal phase HfO_2	Monoclinic phase HfO_2
m_e^*/m_0	0.86; 0.86 (Γ → L) 1.97; 0.68 (Γ → X)	0.72 (Γ → M) 0.94 (Γ → Z)	1.03 (B → A) 1.21 (B → D)
m_h^*/m_0	0.32 (X → Γ) 3.04 (X → W)	0.78 (2) (A → Z) 8.26 (2) (A → M)	0.85 (Γ → Z) 1.28 (Γ → D)

the minimum ($0.68m_0$) and maximum ($1.97m_0$) occuring in cubic HfO_2. The calculated effective masses can be compared with the experimental values of the electron tunneling effective mass in amorphous HfO_2: $m_e^* = 0.22m_0$ [1], $m_e^* = 0.1m_0$ [79], $m_e^* = (0.15-0.23)\,m_0$ [80], and $m_e^* = 0.17m_0$ [81].

Shown in Fig. 15 is the PDOS calculated for 4f, 5p, and 5d oxygen orbitals for cubic, tetragonal, and monoclinic HfO_2. The Hf 6s density of states is not shown because it contributes negligibly to the formation of the electron density. It can be seen that for all three crystalline phases of HfO_2, the Hf and O electronic orbitals enter in equal proportions into the spectrum of electronic states. In the conduction band, the density of states is primarily formed from transition metal d states, i.e., from the 5d states of Hf. The upper subband of the valence band is mainly formed from oxygen 2p states with a certain contribution from Hf 5d states; the middle, from Hf 4f states with an admixture of oxygen 2s states; and the lower, virtually completely from Hf 5p states. The similar nature of the electronic structure of the cubic, tetragonal and monoclinic phases of HfO_2 points to the fact that the properties of HfO_2 are determined by the short-range order in the atomic arrangement.

In Fig. 16, we compare the experimental spectra of amorphous HfO_2 (X-ray, excitation by 1486.6 eV; UV, excitation by 40.8 eVquanta; and photoelectrons) with corresponding calculated spectra for monoclinic HfO_2. The calculated curves are obtained by summing the partial densities of states of the 5p, 4f, 5d, and 6s orbitals of Hf and 2s orbitals of O; the required photoionization cross sections are taken from Ref. [60]. Comparison of the experimental XPSs with the calculated spectra shows good qualitative

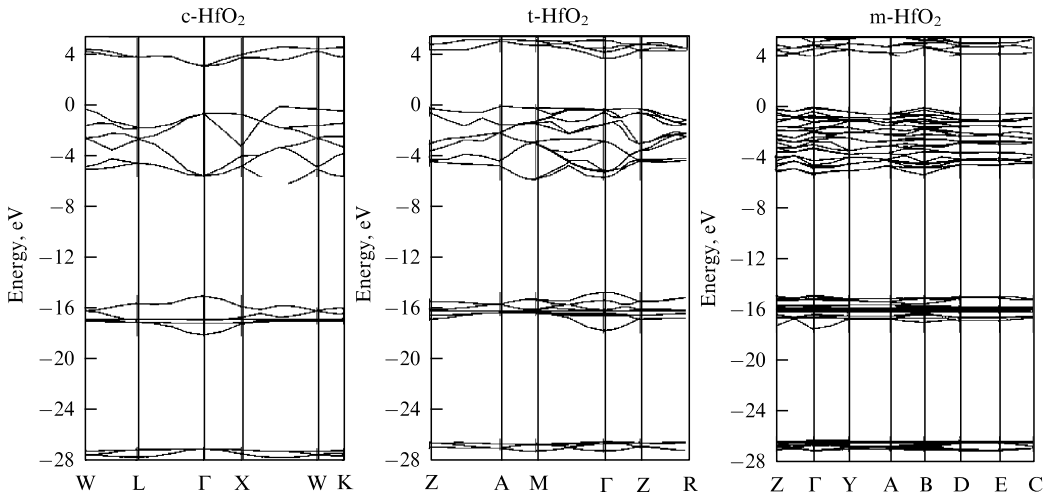

Figure 14. Band diagrams of cubic, tetragonal, and monoclinic HfO_2 along the special symmetry points of the corresponding Brillouin zones.

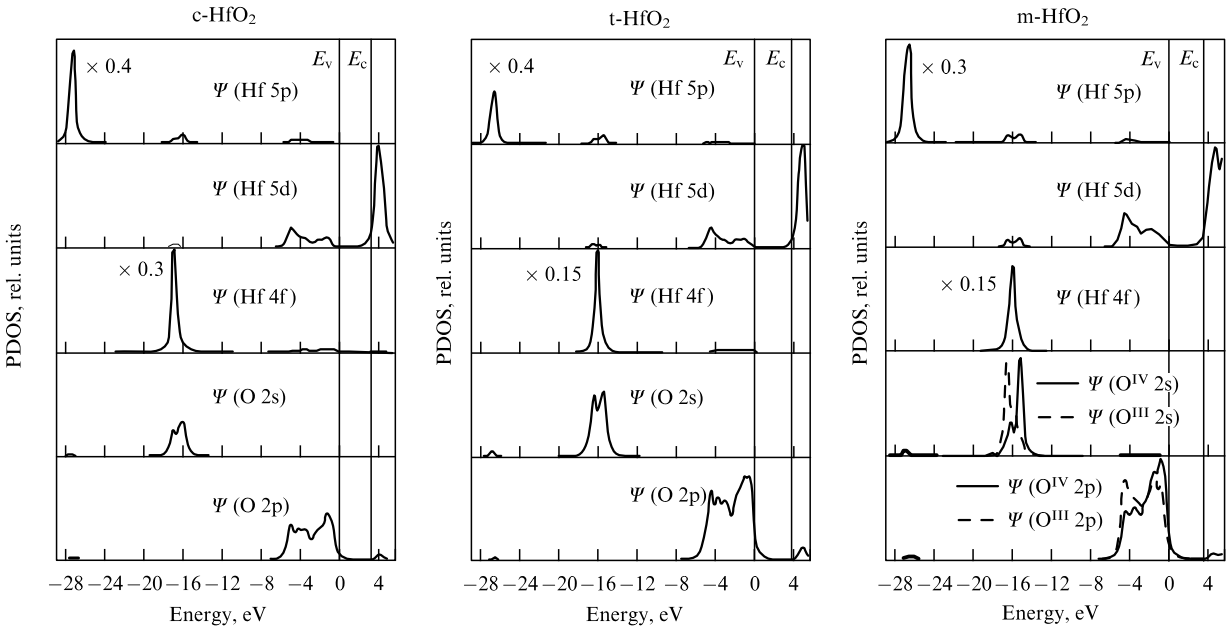

Figure 15. Calculated partial densities of states for cubic, tetragonal, and monoclinic HfO_2 for 4f, 5p, and 6d orbitals of Hf and 2s and 2p orbitals of O. The spectra are broadened by a Lorentzian with the halfwidth $\sigma = 0.2$ eV.

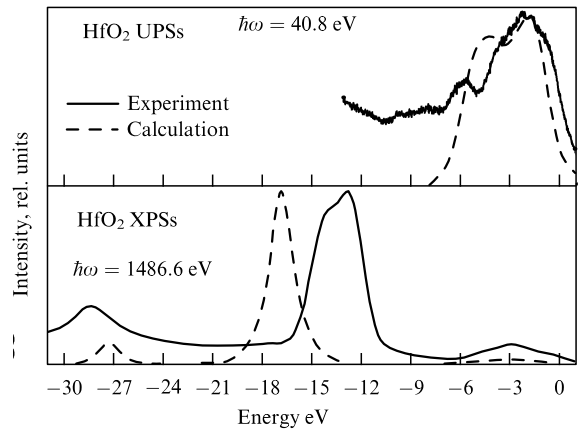

Figure 16. Experimental UPSs and XPSs of amorphous HfO_2 (solid lines) and the corresponding calculated spectra of monoclinic HfO_2 (dashed lines).

agreement. There are three valence subbands separated by ionic gaps. The peaks of the experimental XPSs (at energies ≈ 3, ≈ 13, and ≈ 28.5 eV) and those of the calculated XPS curves (at the same energies) are seen to agree in their relative intensities. The dominant contribution to the experimental UPSs comes from 2p states. The calculated UPSs clearly show two main peaks (at ≈ 1.5 and ≈ 4.5 eV), in agreement with the experimental curve (energies ≈ 1.5 and ≈ 5.5 eV). However, the relative intensities of the main peaks for the calculated and experimental curves agree poorly. Similarly to Al_2O_3, the difference in width between calculated and experimental peaks is due to the broadening of the experimental peaks, and the mismatch in peak positions is due to the underestimated calculated widths of all the subbands of the valence band. Still, the calculated and experimental photoelectron spectra of crystalline and amorphous HfO_2 can be considered to be in satisfactory agreement. This leads to the conclusion that DFT band calculations for the cubic, tetragonal, and monoclinic phases of HfO_2 give a qualitatively correct picture of the valence band.

According to Ref. [82], the three allotropic modifications of HfO_2 have electronic structures similar to those of the corresponding modifications of ZrO_2. The reason is that Zr and Hf are isoelectronic elements (that is, they have the identical structure of the valence shell).

6. Electronic structure of TiO_2

Titanium dioxide (TiO_2, $\varepsilon \approx 80$) is a promising candidate for a subgate dielectric in MIS structures with a small channel length (32.20 nm). Three natural polymorphs of TiO_2 are rutile, anatase, and brookite. Rutile is the most common stable crystalline form of TiO_2. Moreover, rutile has the simplest and most studied crystal structure. The electronic structure of rutile has been the subject of intensive study, both theoretical [83 – 91] and experimental [92 – 94].

The crystal structure of rutile can be described by a tetragonal unit cell ($P4/mnm$) with crystal parameters $a = b = 4.59$ Å and $c = 2.959$ Å [84]. The unit cell of rutile contains two Ti atoms six-fold coordinated by O atoms and four O atoms three-fold coordinated by Ti atoms (Fig. 17a). A Ti atom has four nearest O atoms at the distance 1. 945 Å and two next-nearest O atoms at 1.985 Å.

The electronic structure of rutile is calculated with the program package ESPRESSO. The electronic configurations of Ti and O are respectively [Ne] $3s^2 3p^6 4s^2 3d^2$ and [He] $2s^2 2p^4$. The core electrons are taken into account by introducing ultrasoft pseudopotentials with a GGA exchange-correlation functional with the Perdew–Wang (PW91) parameterization.

The calculated band spectrum of rutile is shown in Fig. 18. The zero of energy is chosen at the top of the valence band. The valence band of rutile consists of two subbands separated by an ionic gap of 9.6 eV. The respective widths of the upper and lower subbands are 5.6 eV and 1.8 eV. According to the calculations, rutile is a direct gap insulator, with the top of the

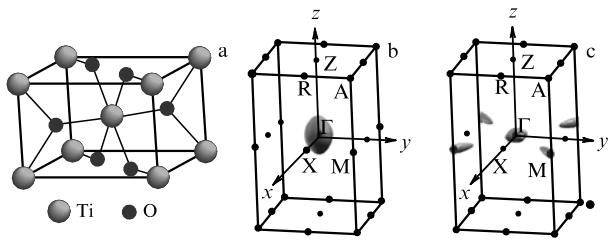

Figure 17. Tetragonal unit cell of rutile (a) and its first Brillouin zone showing its symmetry points and the constant-energy surface near the top of the valence band (b) and near the bottom of the conduction band (c).

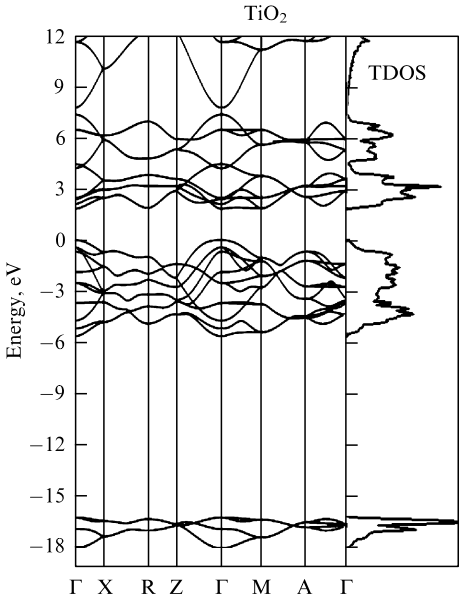

Figure 18. Band spectrum of rutile calculated for the high-symmetry points of the Brillouin zone.

valence band and the bottom of the conduction band at the Γ point of the Brillouin zone. However, another minimum occurs at the M point, 28 eV above that at the Γ point. The value of 28 MeV is, in practical terms, equal to the result of 30 MeV [88] obtained using the linear combination of muffin-tin orbitals (LMTO) method. The obtained results are in agreement with the experimental facts [94] that rutile is a direct-gap material and that its conduction band is virtually degenerate, with minima E_c 15 MeV apart.

The band gap width calculated from the energy difference between the last filled and first free states is 1.9 eV. This result agrees well with previous calculations [87–90]. The experimental values of E_g for rutile lie in the range 3.0–3.1 eV [92–95]. Interestingly, the gap width estimate from Eqn (4.1) is identical to the experimental value $E_g = 3.1$ eV.

Table 3 provides the maximum and minimum calculated values of the electron (m_e^*) and hole (m_h^*) effective masses along some Brillouin zone directions in crystalline rutile. Both electrons and holes exhibit large anisotropy in their effective masses. It is seen that there are both heavy electrons ($1.2m_0$ in the $\Gamma \rightarrow$ M direction) and light electrons ($0.5m_0$ in the $\Gamma \rightarrow$ Z direction) in the crystal. In Ref. [96], the electron effective mass in a rutile crystal was measured to be $m_e^* = 3m_0$. The value of the tunneling effective mass $m_e^* = 0.5m_0$ is given in Ref. [97]. Experimental values of the hole effective masses in

Table 3. Maximum and minimum values of the electron (m_e^*) and hole (m_h^*) effective masses in rutile TiO_2.

	Rutile TiO_2
m_e^*/m_0	1.2 ($\Gamma \rightarrow$ M) 0.5 ($\Gamma \rightarrow$ Z)
m_h^*/m_0	2.8 ($\Gamma \rightarrow$ X) 4.8 ($\Gamma \rightarrow$ Z)

TiO_2 are not available in the literature. According to calculations, holes in a rutile crystal are heavy: $m_h^* \geqslant 2.8m_0$.

The constant energy surface in k space near the top of the valence band is an ellipsoid stretched along the z axis. (Fig. 17b). As a consequence, the hole effective masses are minimum along this axis and isotropic in the xy plane. The energy surface near the bottom of the conduction band is flattened out along the z axis (Fig. 17c), and the electron effective masses are maximum in this direction. In the xy plane, in the $\Gamma \rightarrow$ M direction (110), the constant energy surface is seen to be the steepest and, accordingly, the electron effective mass is at its minimum (which is $0.5m_0$). In the $\Gamma \rightarrow$ X direction (100), the electron effective mass is slightly less than the maximum value, $m_e^* = 1.2m_0$.

Figure 19 shows the partial densities of states calculated for the conduction band and for two valence subbands in a rutile crystal. The partial densities of the Ti 2s and Ti 2p states contribute little to the electronic structure of the valence band and are therefore not shown. It follows that similarly to most transition metal oxides, the conduction band states of rutile are primarily formed from the d states of a transition metal,

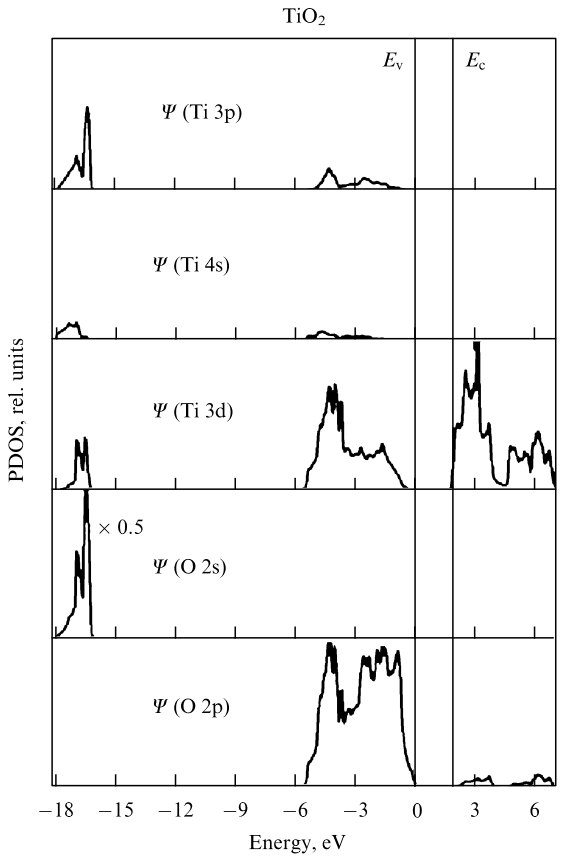

Figure 19. Calculated partial densities of states for 4s, 3p, and 3d orbitals of Ti and 2s and 2p orbitals of O in rutile.

i.e., by the 3d orbitals of Ti. The calculated results for the spatial distribution of the charge density show that the bottom of the conduction band of rutile is formed by nonbinding Ti d orbitals. The upper valence subband mainly consists of O 2p states (with a noticeable contribution from Ti 5d states), although the top of the valence band is formed exclusively by 2p electron states of O. The distribution pattern of the charge density in a rutile crystal shows that the top of its valence band is formed by nonbinding oxygen $2p_\pi$ orbitals. These results agree well with other studies of the electronic structure of rutile [83, 85, 89], and, in addition, similar features are observed in the anatase crystal [98]. In the middle of the valence band, oxygen 2p states strongly overlap with Ti 3d states with a small contribution from Ti 3p and Ti 4s. The charge distribution along the Ti – O bond in the midgap energy range points to the presence of a binding σ orbital. The lower narrow subband is formed from oxygen 2s states with a small admixture of Ti 3d and Ti 3p states.

The calculated spectrum of the total phonon density of states at the Γ point in k space shows that TiO_2, like Al_2O_3, has low-frequency phonon modes that are responsible for the high value of the static dielectric constant. The electronic component of the dielectric tensor ε_{ij}^{e} of TiO_2 takes the following form in Cartesian coordinates:

$$\varepsilon_{ij}^{\infty}(TiO_2) = \begin{pmatrix} 7.4 & 0.0 & 0.0 \\ 0.0 & 7.4 & 0.0 \\ 0.0 & 0.0 & 9.0 \end{pmatrix}.$$

This result confirms the well-known anisotropy of the optical properties of rutile. The values $\varepsilon_{xx}^{\infty} = \varepsilon_{yy}^{\infty} = 7.4$ and $\varepsilon_{zz}^{\infty} = 9.0$ agree satisfactorily with the experimental values for the 'usual' ($n_{\text{usual}} = 2.63$) and 'unusual' ($n_{\text{unusual}} = 2.89$) refractive index of rutile [80].

Figure 20 presents the experimental electron energy loss spectra (EELSs) of amorphous TiO_2 under a monochromatic 200 eV electron beam. The zero energy is the energy of elastically reflected electrons. The band gap width is estimated to be $E_g \leqslant 3.7$ eV. Losses at the energies 6.9, 15.0, and 46.9 eV correspond to the excitation of the valence electrons of rutile. The maximum of the energy loss spectrum gives $\hbar\omega_p = 22.8$ eV for the bulk plasmon energy. It is interesting to compare this value with the simple free electron gas estimate

$$\hbar\omega_p = \hbar\left(\frac{4\pi N e^2}{m_e^*}\right)^{1/2}, \qquad (6.1)$$

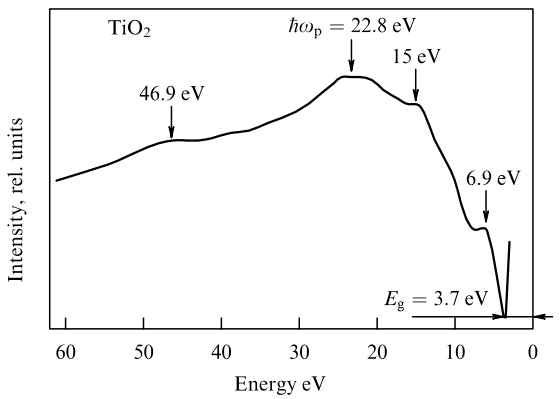

Figure 20. Characteristic electron energy loss spectrum in amorphous TiO_2. Incident beam energy is 200 eV.

where N is the concentration of valence electrons participating in plasma oscillations. The electron effective mass m_e^* can be taken equal to the free electron mass because there are no intensive interband transitions near a plasma resonance [99]. The inclusion of oxygen 1p and Ti 3d and 4s valence electrons yields the estimate $\hbar\omega_p = 24.04$ eV, which is close to the measured value 22.8 eV. But if oxygen 2s electrons are also assumed to participate in plasma oscillations, then the plasmon energy is estimated to be $\hbar\omega_p = 26.61$ eV.

7. Conclusion

We have reviewed the atomic and electronic structure of Al_2O_3, HfO_2, and TiO_2, three of the most important and promising high-k dielectrics. The experimental X-ray emission spectra, calculated PDOS spectra, and spatial charge density distribution in the valence band of Al_2O_3 indicate that the top of the valence band is primarily formed by nonbinding oxygen $2p_\pi$ states. The calculated spatial charge density distribution in the rutile crystal also shows that the top of the valence band is formed by nonbinding oxygen $2p_\pi$ states. This is the most likely reason for large values of the hole effective masses in both Al_2O_3 and TiO_2. For α- and γ-Al_2O_3, it is established that close to the top and in the middle of the valence band, in addition to nonbinding oxygen $2p_\pi$ states, there are also oxygen 2p and Al 3s and 3p states, corresponding to light holes with the effective mass $m_h^* \approx 0.35-1.3m_0$. For TiO_2, binding orbitals exist only below the top of the valence band, and hence light holes are not observed in the rutile crystal. We note that a similar picture is observed in well-studied SiO_2 and Si_3N_4.

In all three materials studied, the calculated electron effective masses lie in the range from $0.4m_0$ to $1m_0$, whereas the hole effective masses are on average much larger. This implies that the conductivity of these materials is dominated by the electron component.

It is established that α-Al_2O_3 and γ-Al_2O_3 have qualitatively similar electronic structures. Similarly, the electronic structures of cubic, tetragonal, and monoclinic HfO_2 are also qualitatively similar. It can be concluded that the electronic properties of both Al_2O_3 and HfO_2 are determined by a short-range order in the atomic arrangement, i.e., (primarily) by the species of the atoms and by their coordination. This conclusion is a reliably established fact for silicon oxides and nitrides [100]. Most likely, this property is a characteristic feature of all semiconductors and all metal oxides.

Although the studied material are promising for modern silicon microelectronics, the in practical use in devices is highly problematic. The reason is that real samples of these materials contain a high concentration of defect states that act as traps for charge carriers. The nature (that is, the atomic and electronic structure) of traps responsible for the localization of electrons and holes in high-k dielectrics is still an open question.

Acknowledgements. This work was supported by the Integration Project No. 70 of the Siberian Branch of the Russian Academy of Sciences; the RFBR project No. 10-07-0053; and the Republic of Korea National Program for Tera-Level Nanodevices. The calculations were in part performed using the NKS-160 cluster at the Siberian supercomputer center of the RAS SB. The useful discussions with A V Shaposhnikov are appreciated.

References

1. Hohenberg P, Kohn W *Phys. Rev.* **136** B864 (1964)
2. Kohn W, Sham L J *Phys. Rev.* **140** A1133 (1965)
3. Kohn W *Rev. Mod. Phys.* **71** 1253 (1999); *Usp. Fiz. Nauk* **172** 336 (2002)
4. Yeo Y-C, King T-J, Hu C *IEEE Trans. Electron Dev.* **50** 1027 (2003)
5. Kingon A I, Maria J-P, Streiffer S K *Nature* **406** 1032 (2000)
6. Robertson J *Eur. Phys. J. Appl. Phys.* **28** 265 (2004)
7. Gritsenko V A et al. *Solid-State Electron.* **47** 1651 (2003)
8. Roizin Y, Gritsenko V, in *Dielectric Films for Advanced Microelectronics* (Eds M Baklanov, M Green, K Maex) (Chichester: John Wiley and Sons, 2007) p. 251
9. Gritsenko V A et al. *Fiz. Tekh. Poluprovod.* **39** 748 (2005) [*Semicond.* **39** 716 (2005)]
10. Gritsenko V A et al. *Microelectron. Eng.* **81** 530 (2005)
11. Bu J, White M H *Solid-State Electron.* **45** 47 (2001)
12. Lee C-H, Park K-C, Kim K *Appl. Phys. Lett.* **87** 073510 (2005)
13. Lisiansky M et al. *Appl. Phys. Lett.* **89** 153506 (2006)
14. Chen S-C et al. *Appl. Phys. Lett.* **91** 193103 (2007)
15. Lai S-C et al. *IEEE Electron Dev. Lett.* **28** 643 (2007)
16. Cheng C H, Lee J Y-M *Appl. Phys. Lett.* **91** 192903 (2007)
17. Lee C-H et al. *Appl. Phys. Lett.* **86** 152908 (2005)
18. Specht M et al. *Appl. Phys. Lett.* **84** 3076 (2004)
19. Wang X, Kwong D-L *IEEE Trans. Electron Dev.* **53** 78 (2006)
20. Gritsan N P *Kvantovaya Khimiya* (Quantum Chemistry) (Novosibirsk: Izd. NGU, 2001)
21. Payne M C et al. *Rev. Mod. Phys.* **64** 1045 (1992)
22. Quantum ESPRESSO, http://www.quantum-espresso.org/
23. Baroni S et al., Plane-Wave Self-Consistent Field, http://www.pwscf.org
24. BAND2004.01, SCM, Theoretical Chemistry, Vrije Universiteit, Amsterdam, The Netherlands, http://www.scm.com
25. Levin I, Brandon D *J. Am. Ceram. Soc.* **81** 1995 (1998)
26. Ritala M et al. *Science* **288** 319 (2000)
27. Brytov I A, Romashchenko Yu N *Fiz. Tverd. Tela* **20** 664 (1978) [*Sov. Phys. Solid State* **20** 384 (1978)]
28. O'Brien W L et al. *Phys. Rev. B* **47** 15482 (1993)
29. Hoffman A, Paterson P J K *Appl. Surf. Sci.* **93** 301 (1996)
30. French R H, Mullejans H M, Jones D J *J. Am. Ceram. Soc.* **81** 2549 (1998)
31. Arakawa E T, Williams M W *J. Phys. Chem. Solids* **29** 735 (1968)
32. Balzarotti A, Bianconi A *Phys. Status Solidi B* **76** 689 (1976)
33. French R H *J. Amer. Ceram. Soc.* **73** 477 (1990)
34. Evarestov R A, Ermoshkin A N, Lovchikov V A *Phys. Status Solidi B* **99** 387 (1980)
35. Barta I P *J. Phys. C* **15** 5399 (1982)
36. Ciraci S, Batra I P *Phys. Rev. B* **28** 982 (1983)
37. Salasco L et al. *Mol. Phys.* **72** (2) 267 (1991)
38. Ching W Y, Xu Y N *J. Am. Ceram. Soc.* **77** 404 (1994)
39. Guo J, Ellis D E, Lam D J *Phys. Rev. B* **45** 3204 (1992)
40. Xu Y-N, Ching W Y *Phys. Rev. B* **43** 4461 (1991)
41. Mo S-D, Ching W Y *Phys. Rev. B* **57** 15219 (1998)
42. Holm B et al. *Phys. Rev. B* **59** 12777 (1999)
43. Lee C-K et al. *Phys. Rev. B* **76** 245110 (2007)
44. Montanari B et al. *Int. J. Quantum Chem.* **106** 1703 (2006)
45. Perevalov T V et al. *Pis'ma Zh. Eksp. Teor. Fiz.* **85** 197 (2007) [*JETP Lett.* **85** 165 (2007)]
46. Ealet B et al. *Thin Solid Films* **250** 92 (1994)
47. Mo S D, Xu Y N, Ching W Y *J. Am. Ceram. Soc.* **80** 1193 (1997)
48. Wolverton C, Hass K C *Phys. Rev. B* **63** 024102 (2000)
49. Gutiérrez G, Taga A, Johansson B *Phys. Rev. B* **65** 012101 (2001)
50. Cai S-H et al. *Phys. Rev. B* **67** 224104 (2003)
51. Paglia G et al. *Phys. Rev. B* **71** 224115 (2005)
52. Pinto H P, Nieminen R M, Elliott S D *Phys. Rev. B* **70** 125402 (2004)
53. Allan D C, Teter M P *Phys. Rev. Lett.* **59** 1136 (1987)
54. Chelikowsky J R, Schlüter M *Phys. Rev. B* **15** 4020 (1977)
55. Kerber A et al. *IEEE Trans. Electron Dev.* **50** 1261 (2003)
56. Kim J et al. *Appl. Phys. Lett.* **80** 2734 (2002)
57. Shu Q Q, Ma W G *Appl. Phys. Lett.* **61** 2542 (1992)
58. Gritsenko V A *Stroenie i Elektronnaya Struktura Amorfnykh Dielektrikov v Kremnievykh MDP Strukturakh* (Atomic and Electronic Structure of Amorphous Insulators in Silicon MIS Structures) (Novosibirsk: Nauka, 1993)
59. Gritsenko V A et al. *Fiz. Tekh. Poluprovod.* **35** 1041 (2001) [*Semicond.* **35** 997 (2001)]
60. Gritsenko V A, Ivanov R M, Morokov Yu N *Zh. Eksp. Teor. Fiz.* **108** 2216 (1995) [*JETP* **81** 1208 (1995)]
61. Yeh J-J *Atomic Calculation of Photoionization Cross-Sections and Asymmetry Parameters* (Amsterdam: Gordon and Breach Sci. Publ., 1993)
62. Loong C K *J. Eur. Cer. Soc.* **19** 2241 (1999)
63. Griscom D L *J. Non-Cryst. Solids* **24** 155 (1977)
64. Afanas'ev V V et al. *J. Appl. Phys.* **91** 3079 (2002)
65. Gignac W J, Williams R S, Kowalczyk S P *Phys. Rev. B* **32** 1237 (1985)
66. Ruh R et al. *J. Am. Ceram. Soc.* **4** 27 (1968)
67. Zheng J X et al. *Phys. Rev. B* **75** 104112 (2007)
68. Foster A S et al. *Phys. Rev. B* **65** 174117 (2002)
69. Holgado J P et al. *Thin Solid Films* **389** 34 (2001)
70. Aarik J et al. *Thin Solid Films* **408** 97 (2002)
71. Manory R R et al. *J. Vac. Sci. Technol. A* **20** 549 (2002)
72. Schaefer J et al. *J. Electrochem. Soc.* **150** 67 (2003)
73. Wang J, Li H P, Stevens R *J. Mater. Sci.* **27** 5397 (1992)
74. Demkov A A *Phys. Status Solidi B* **226** 57 (2001)
75. Zafar S et al. *Appl. Phys. Lett.* **67** 1031 (1995)
76. Afanas'ev V V et al. *Appl. Phys. Lett.* **81** 1053 (2002)
77. Kato H et al. *J. Appl. Phys.* **92** 1106 (2002)
78. Perevalov T V et al. *J. Appl. Phys.* **101** 053704 (2007)
79. Zhu W J et al. *IEEE Electron Dev. Lett.* **23** 97 (2002)
80. Hinkle C L et al. *Surf. Sci.* **566 – 568** 1185 (2004)
81. Takeuchi H, King T-J *Appl. Phys. Lett.* **83** 788 (2003)
82. Perevalov T V et al., in *Defects in High-k Gate Dielectric Stacks* (Ed. E Gusev) (Dordrecht: Springer, 2006)
83. Lawler H M et al. *Phys. Rev. B* **78** 205108 (2008)
84. Schelling P K, Yu N, Halley J W *Phys. Rev. B* **58** 1279 (1998)
85. Fahmi A F et al. *Phys. Rev. B* **47** 11717 (1993)
86. Lin L B, Mo S D, Lin D L *J. Phys. Chem. Solids* **54** 907 (1993)
87. Mo S-D, Ching W Y *Phys. Rev. B* **51** 13023 (1995)
88. Reinhardt P, Hess B A *Phys. Rev. B* **50** 12015 (1994)
89. Glassford K M, Chelikowsky J R *Phys. Rev. B* **46** 1284 (1992)
90. Glassford K M, Chelikowsky J R *Phys. Rev. B* **45** 3874 (1992)
91. Poumellec B, Durham P J, Guo G Y *J. Phys. Condens. Matter* **3** 8195 (1991)
92. Amtout A, Leonelli R *Phys. Rev. B* **51** 6842 (1995)
93. Fischer D W *Phys. Rev. B* **5** 4219 (1972)
94. Pascual J, Camassel J, Mathieu H *Phys. Rev. B* **18** 5606 (1978)
95. Yamamoto S et al. *Thin Solid Films* **401** 88 (2001)
96. Pascual J, Camassel J, Mathieu H *Phys. Rev. Lett.* **39** 1490 (1977)
97. Mikhelashvili V, Eisenstein G *J. Appl. Phys.* **89** 3256 (2001)
98. Asahi R et al. *Phys. Rev. B* **61** 7459 (2000)
99. Philipp H R, Ehrenreich H *Phys. Rev.* **129** 1550 (1963)
100. Gritsenko V A, in *Nitrid Kremniya v Elektronike* (Silicon Nitride in Electronics) (Novosibirsk: Nauka, 1982) [Translated into English (New York: Elsevier, 1988)]